International Journal of Engineering and Technology Innovation, vol. 14, no. 4, 2024, pp. 335-354

Analysis of Atomization Performance of Linear Laval Nozzle under Varied Water Pressures Based on VOF and DPM Models

Shanshan Tang[1,2], Mohd Danial Ibrahim[2,*], Andrew Ragai Henry Rigit[2], Wei Zhang[3], Chaokun Wei[4]

[1]Faculty of Engineering, Anhui SanLian University, Hefei, China

[2]Faculty of Engineering, University of Malaysia Sarawak, Kota Samarahan, Sarawak, Malaysia

[3]Dongguan Mistec Spraying Technology Co., Ltd., Dongguan, China

[4]Chery Automobile Corporation, Wuhu, China

Received 23 April 2024; received in revised form 04 June 2024; accepted 05 June 2024

DOI: https://doi.org/10.46604/ijeti.2024.13615

Abstract

Particulate matter from coal and stone operations is a primary air pollution source. The traditional nozzle requires high-pressure conditions, and the atomization droplets are large and uneven. This paper aims to study a linear Laval nozzle and investigate the impact of water pressure on atomization performance. The volume of fluid (VOF) model and discrete phase model (DPM) of Fluent are used to simulate the internal and external fields of the nozzle and analyze the velocity, droplet size, and atomization angle. The results show that the optimized water pressure parameters are 0.1 MPa with an air pressure of 0.5 MPa. Droplets in the middle are smaller, while those on the sides are larger. Compared to traditional nozzles, the water pressure is reduced by over 90%, and the Sauter mean diameter (SMD) decreases by over 50%. Moreover, the theoretical spray angle increases by approximately 150%.

Keywords: linear laval nozzle, VOF, DPM, water pressure, atomizing performance

1. Introduction

In recent years, with the rapid development of the economy and the great demand for resources, particulate matter generated during mining, processing, and transportation of coal and stone materials has become one of the primary sources of air pollution. Especially when small particles such as PM2.5 and PM10 diffuse into the atmosphere, it is difficult to capture and remove them again, which will cause significant harm to human health and the environment, attract critical social attention, and threaten human survival [1].

China is rich in coal resources. As of 2020, China's proven coal reserves were 187.55 billion tons, making it the world's largest coal storage country and producer. By 2020, China's annual coal production was 3.84 billion tons, accounting for nearly half of global coal production. Coal mining produces dust, seriously polluting the working environment, and causes occupational diseases such as pneumoconiosis. In China, over 90% of the nearly one million people diagnosed with occupational diseases are occupational pneumoconiosis, and 80% of them work in coal mines. The number of new cases of occupational pneumoconiosis in China from 2017 to 2022 is shown in Fig. 1 [2]. The number is declining. However, there is still a significant number of new cases of occupational pneumoconiosis every year.

Current status of dust removal technology: atomized dust removal technology, clustering-dust removal technology, electric dust removal technology, chemical agglomeration technique, and negative pressure dust removal technology, among which atomized dust removal technology is the most widely used. In the process of atomized dust removal, the probability of dust adsorption and condensation is the largest when the size of atomized droplets is similar to that of dust particles [3].

* Corresponding author. E-mail address: imdanial@unimas.my

English language proofreader: Yen-Chun Hsieh

Numerous researchers have researched the dust removal device. Liu et al. [4], Xu et al. [5], and Xu et al. [6] simulated pressure-swirling nozzles. They got 5 MPa, 6 MPa, and 8 MPa, which are the optimal pressure. Arya et al. [7] proposed a flooded-bed dust scrubber system. On the other hand, Shi et al. [8] simulated coalbed water infection and concluded that an injection pressure of 8 MPa was generally acceptable. Wang et al. [9] investigated X-type swirl pressure nozzles with the feed water pressure in a range of 1-8 MPa. Zhang et al. [10-11] studied a supersonic antigravity siphon atomization nozzle with a curved Laval structure. COMSOL software was employed to simulate the process of droplet crushing and atomization. The results show that curved Laval nozzles surpass the traditional atomizing nozzles in droplet velocity, water pressure, and droplet size.

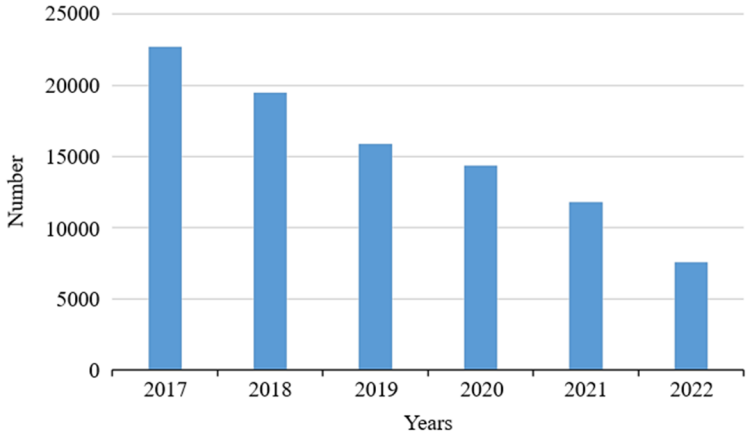

Fig. 1 The number of new cases of occupational pneumoconiosis in China from 2017 to 2022 [2]

Based on the above summary, it is evident that atomization dust removal is currently the primary method for dust control. Traditional nozzles require high pressure, mostly above 5 MPa, which results in high energy consumption and potential safety hazards. In contrast, the Laval nozzle operates at pressures below 1 MPa and produces small, uniform droplets. However, there is currently limited research on using Laval nozzles for dust removal, especially linear ones. The purpose of this paper is to study a linear Laval nozzle and optimize the water pressure.

The Laval model is shown in Fig. 2. The Laval nozzle is a dynamic device that accelerates fluid by converging and diverging its cross-section to reach supersonic speeds, possessing unique dynamic characteristics. Its design is based on the research of Swedish engineer Gustaf de Laval and is widely used in fields such as turbo machinery, rocket propulsion, and jet engines. Still, there is limited research in the dust removal field. Application of Laval nozzles can achieve supersonic atomization effects, as the ejection speed plays a critical role in the atomization process. Therefore, supersonic atomization technology can obtain finer and more concentrated droplet size distributions than conventional air atomization techniques [12-13].

Fig. 2 Laval model [12]

2. Laval Nozzle Structure Design

The Laval nozzle comprises a subsonic contraction section, a critical throat section, and a supersonic expansion section. The general principle of Laval nozzle design is that the pressure energy of the airflow must be effectively converted into kinetic energy. Currently, the internal construction of the Laval nozzle consists of two types: linear and curved. The contraction section

of the curved structure can be designed with the Vitosinski curve. However, the manufacturing cost of the curved surface is high, and the linear surface is easy to process [14]. Therefore, the cone is selected for the contraction section in this research, as shown in Fig. 3.

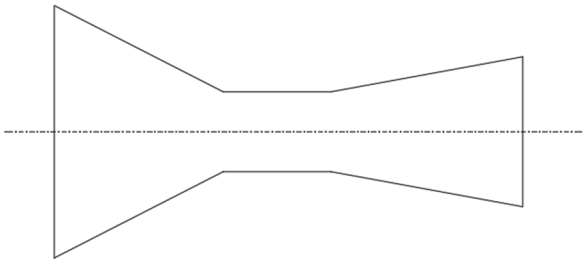

Fig. 3 Linear Laval nozzle

2.1. Expansion section

If the diameter of the throat is d_2, the length of the expansion section and the half-angle of the expansion are L_2 and α, respectively. Then, the diameter of the outlet d_3 is shown as follows:

$$d_3 = 2L_2 \tan\alpha + d_2 \tag{1}$$

The length of the expansion segment L_2 is shown as follows [15]:

$$L_2 = \left(d_3 - d_2\right)/2\tan\alpha \tag{2}$$

Because the airflow completely works in the supersonic range, the friction irreversible loss is too large if the expansion section is too long. Suppose the expansion section is too short or the section expansion is too large. In that case, the airflow will be separated from the wall, resulting in eddy current loss that is unfavorable to energy conversion. As a rule, the expansion half-angle is generally 8° to 15°. According to the literature, the outlet airflow velocity of the Laval nozzle gradually increased within the range of 8° to 10° expansion half-angle. From 11° to 15°, it tends to be stable. It can be seen that the expansion half-angle of 10° is the most appropriate.

2.2. Contraction section

The performance of the contraction section depends on the ratio of the inlet area to the contraction section's outlet area and the contraction section's shape. The diameter of the inlet is d_1. The diameter of the throat is d_2. To accelerate the airflow statically, the cone angle θ of the contraction section is generally 30° to 60° [16], and the length of the contraction section is shown in the formula below. L_1 is usually (3-5) times d_2 (throat diameter).

$$L_1 = \frac{d_3 - d_2}{2} \times \cot\frac{\theta}{2} \tag{3}$$

where, d_1 is the inlet diameter, d_2 is the throat diameter, θ is the cone angle, and L_1 is the length of the contraction section.

2.3. Throat section

The throat is the critical position where the airflow changes from subsonic to supersonic and is the most important part of the entire nozzle design. The actual use of the nozzle requires that the flow rate should not be too small, which requires that the throat diameter should not be too small, generally between 1-2 mm. The nozzle assembly drawing is shown in Fig. 4. The first atomization occurs when the air and water are mixed at the Laval core. Then, the high-speed gas-liquid mixing flow impinges on the oscillator at supersonic speed to produce ultrasonic waves. The high-frequency vibration energy of the ultrasonic wave atomizes the liquid droplet again.

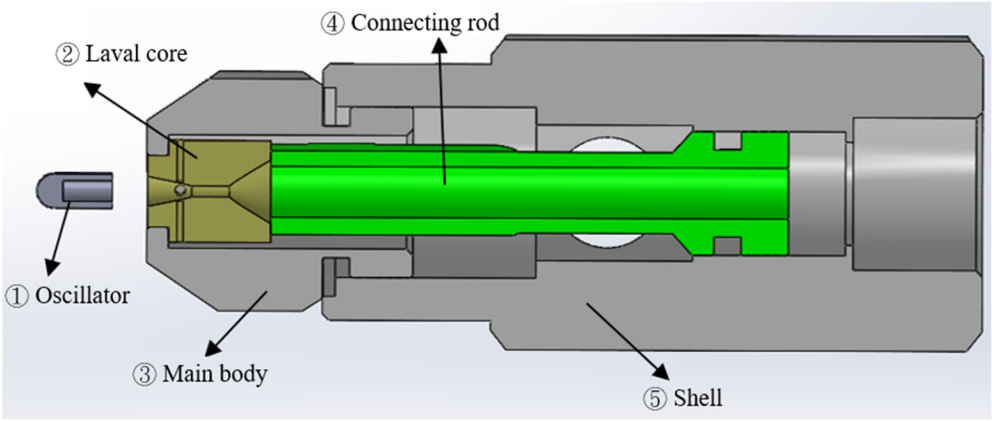

Fig. 4 Nozzle assembly drawing

In the case of high dust concentration, the combined nozzle shown in Fig. 5 can be used. The Laval combined nozzle features six outlets positioned around its perimeter and center, expanding the atomization cone angle. Its flow rate is six times that of a standard Laval nozzle, while also increasing droplet concentration, making it well-suited for environments with high dust concentrations.

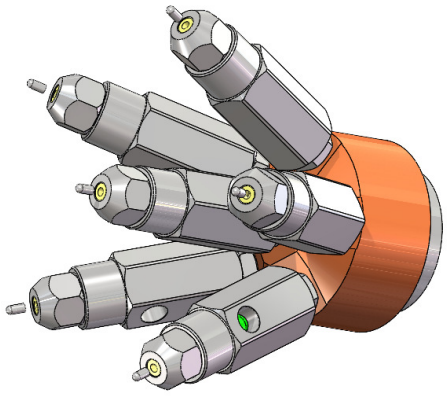

Fig. 5 Laval combined nozzle

3. Numerical Analysis with Varied Water Pressure

The inlet pressure should not be excessively high, as it can easily lead to outlet disturbances. Additionally, high pressure imposes higher demands on equipment and nozzle manufacturing processes. Therefore, in practical usage, priority is given to selecting medium and low-pressure conditions. Furthermore, Laval nozzles exhibit high internal airflow velocities, and medium and low water pressures can achieve excellent atomization effects [17-18]. Here, water pressures of 0.1/0.2/0.3/0.4/0.5 MPa are selected, with an air pressure of 0.5 MPa, a nozzle outlet diameter of 2.5 mm, and a nozzle-to-oscillator distance of 4 mm.

For the Laval gas-liquid two-phase flow nozzle, liquid entering the nozzle cavity is dispersed by high-speed airflow. After the droplet breakup process, the gas-liquid mixture is expelled from the nozzle outlet. This process involves the flow of gas and liquid phases and can be simulated using the volume of fluid (VOF) model to analyze the flow fields inside and outside the nozzle. The VOF model is a type of Eulerian multiphase flow model. In this model, if the volume fraction of a particular fluid within a computational cell is set to 0, it indicates the absence of that fluid in that cell. Conversely, if the volume fraction is set to 1, it denotes the presence of only that fluid in the cell [19].

The discrete phase model (DPM) is used in Fluent to simulate the flow of particles. The DPM model assumes that particles are discrete point-like objects and simulates processes such as particle transport, collision, and deposition by tracking the movement of these particles in the fluid. This model is typically suitable for situations where there is a strong interaction

between particles and the fluid, such as particle transport in air flows or particle sprays. It defines gas as the continuous phase and liquid droplet as the discrete phase. The DPM model can simulate droplet trajectories and display particle sizes. In Fluent, users can simulate various types of particle behavior by setting parameters such as initial position, velocity, and size of the particles. Additionally, users can couple fluid flow conditions, boundary conditions, etc., with particle simulations to obtain information such as particle trajectories, concentration distributions, etc., within the fluid [19].

This study aims to obtain the velocity distribution of the flow field, the spray atomization angle, the volume distribution of water, and the droplet size distribution and numerical values of a linear Laval nozzle. The VOF model is used to calculate the flow field velocity distribution, spray atomization angle, and water volume distribution. The DPM is employed to determine the droplet size distribution and numerical values. Therefore, this study combines the DPM and VOF models to achieve these objectives.

3.1. VOF simulation setup

(1) Governing equation

The governing equations used in the VOF model are shown in the formula below [20].

Continuity equation

$$\frac{\partial \rho}{\partial t}+\nabla \cdot(\rho u)=0 \tag{4}$$

Momentum equation

$$\frac{\partial\left(\rho u_i\right)}{\partial t}+\frac{\partial\left(\rho u_i u_j\right)}{\partial i}=\frac{\partial \rho}{\partial x_i}+\frac{\partial u}{\partial x_i} \times\left(\frac{\partial \rho}{\partial x_i}+\frac{\partial u}{\partial x_i}\right)+\rho g_i+F_j^{\prime} \tag{5}$$

Volume fraction transport equation

$$\frac{\partial F}{\partial t}+u_i \frac{\partial F}{\partial x_i}=0 \tag{6}$$

where,

$$\rho=F \rho_1+(1-F) \rho_2 ; \ u_i=F u_{i 1}+(1-F) u_{i 2} \tag{7}$$

Here, ρ represents density, kg/m^3; F' represents body forces due to external actions, N; F represents volume fraction; i, j are tensor indices; u represents flow velocity, m/s; t represents time, s; x represents coordinates, m; g represents acceleration of gravity, m/s^2.

(2) Domain and boundary conditions

The air pressure is 0.5 MPa, and the water pressure varies from 0.1 MPa to 0.5 MPa. The external flow field measures 1500 mm in length and 600 mm in width. Fig. 6 illustrates both the internal and external flow fields of the nozzle. Fig. 7 provides an enlarged view of the flow field around the nozzle.

Fig. 6 Internal and external flow fields of the nozzle

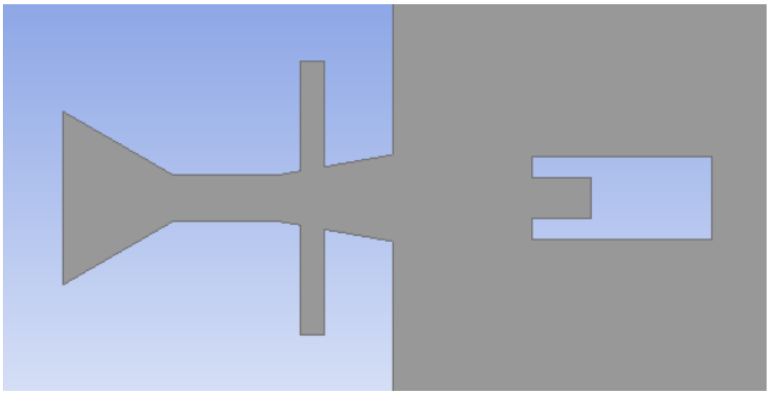

Fig. 7 An enlarged view of the flow field around the nozzle

The operating pressure is 101325 Pa. Fig. 8 illustrates the boundary conditions for external flow fields. On the left side of the external flow field, it is set as a Pressure-far-field, with the pressure being 0 MPa. It is set as a pressure outlet on the right side, with the pressure being 0 MPa. The acoustic wave model employed is non-reflecting.

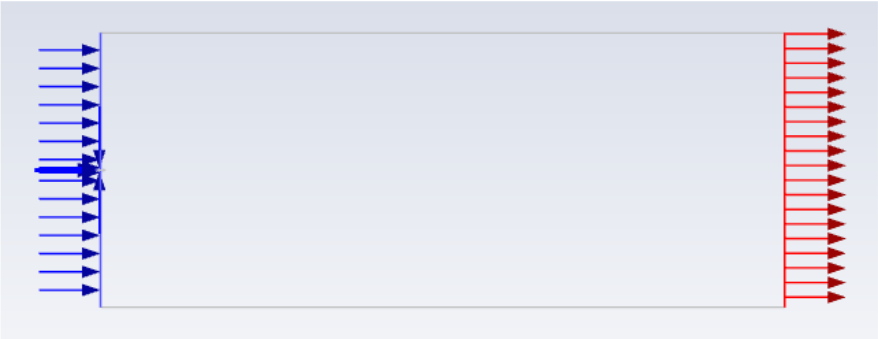

Fig. 8 Boundary conditions for external flow fields

Air is a primary phase; water is a secondary phase. The boundary conditions of the nozzle section are set, as shown in Fig. 9. The air inlet is on the left side, and the type is pressure inlet. The volume fraction of water is 0. The pressure is 0.5 MPa. They act as water inlets on the top and bottom sides, set as pressure inlets. The water volume fraction is set to 1, with pressure settings ranging from 0.1 to 0.5 MPa. All other boundaries are treated as walls.

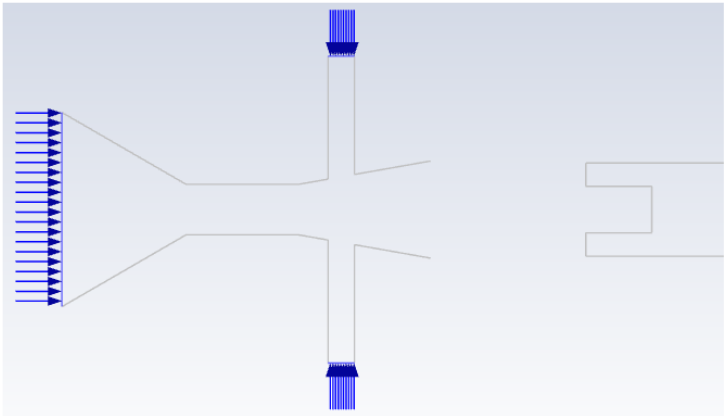

Fig. 9 Boundary conditions for nozzle

(3) Meshing and setting up

(3-1) Meshing

Triangular meshes are well-suited for complex and irregular geometries, making them easier to divide into irregular areas and sharp corners. This flexibility is particularly advantageous when handling intricate models. Additionally, triangular meshes exhibit good stability and convergence during the solving process, leading to their widespread use in many engineering and

scientific computations [21]. Therefore, this study employs triangular meshes. The meshing was performed using the Fluent-Mesh module, the domains comprised 137482 unstructured triangle elements and 73864 nodes. Element size is 0.004 m. The mesh for the nozzle's internal and external fluid regions is shown in Fig. 10.

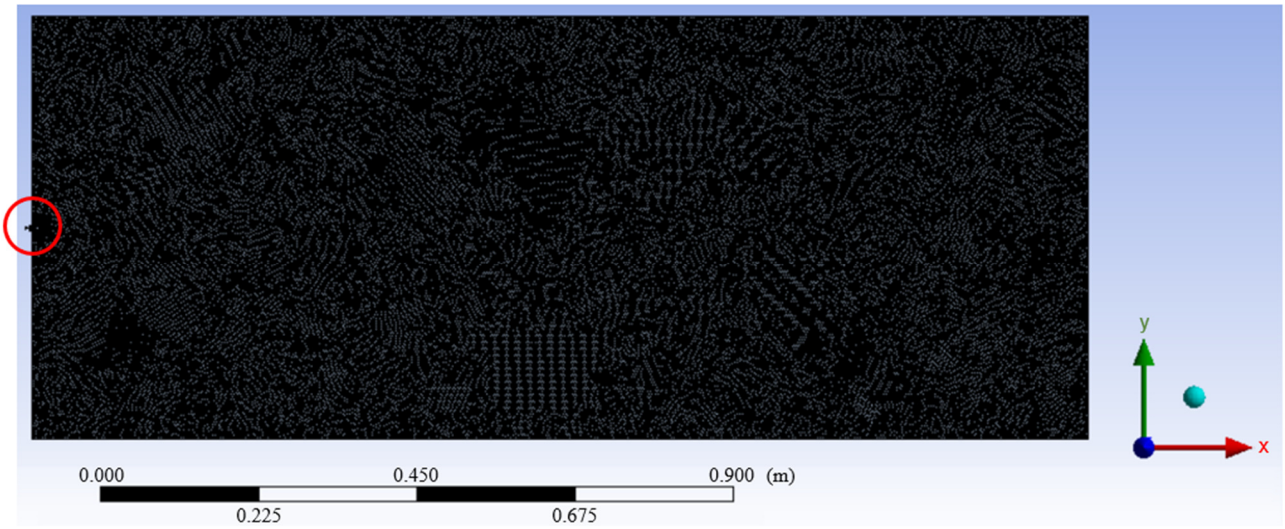

Fig. 10 The mesh for the internal and external fluid regions of the nozzle

The mesh surrounding the nozzle is depicted in Fig. 11. The mesh inside the nozzle is displayed as shown in Fig. 12. The boundary layer's inflation is illustrated as shown in Fig. 13. The inflation option is total thickness. The number of layers is 5, the growth rate is 1.05, and the maximum thickness is 0.0005. The average orthogonal quality is excellent, with 0.9586.

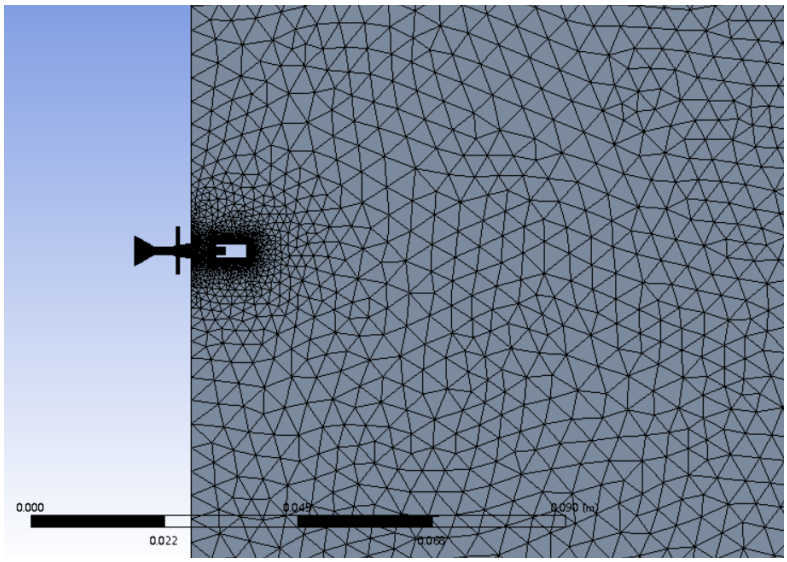

Fig. 11 The mesh surrounding the nozzle

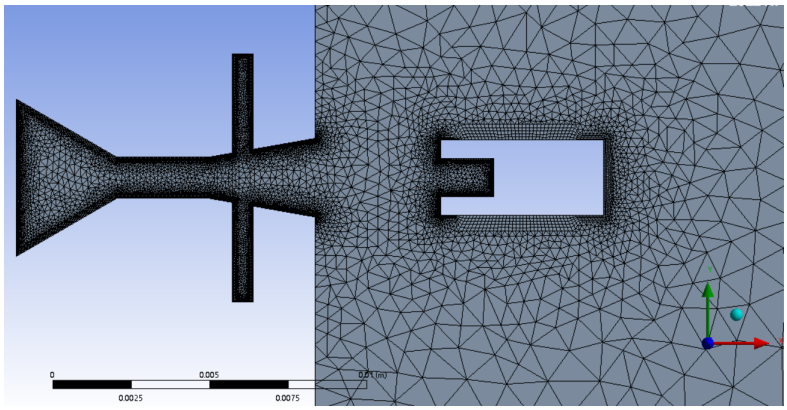

Fig. 12 The mesh inside the nozzle

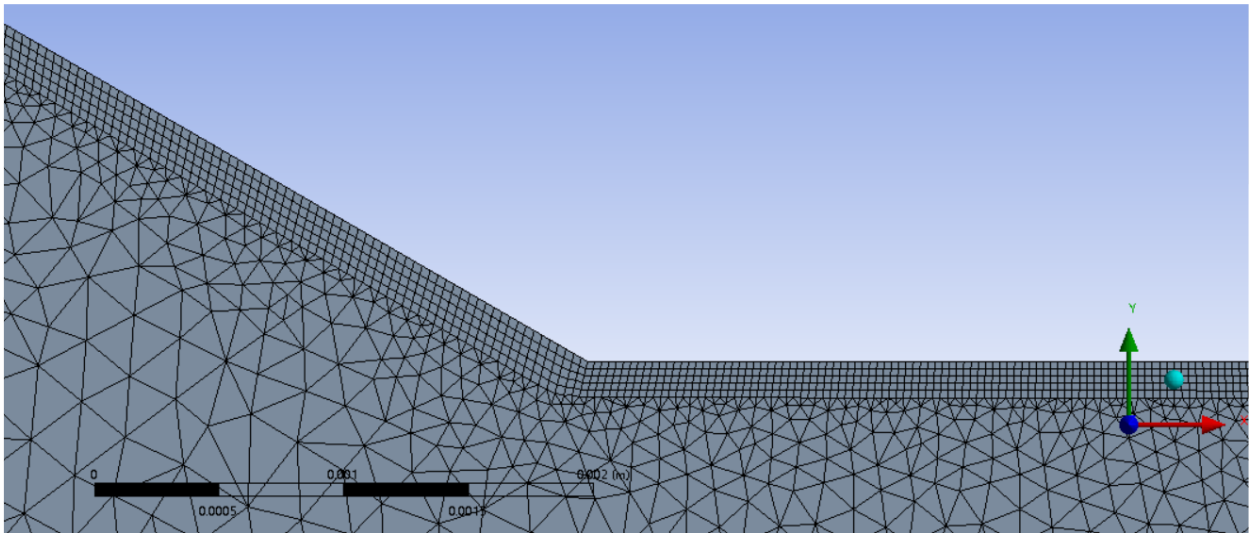

Fig. 13 The boundary layer's inflation

(3-2) Mesh independence test

This section examines the impact of the total number of grids on computational results. The grid independence test, conducted under conditions of 0.5 MPa air pressure and 0.1 MPa water pressure, is presented in Table 1. As shown in Table 1, variations in the number of grids have some effect on the computational results within a certain range. However, the overall deviation is within 0.5%, meeting the requirements for grid independence. Considering computational accuracy and efficiency, the total number of grids is ultimately set at 137,482 for the mesh division.

Table 1 The grid independence test with varied element size

Number	Element size (m)	Elements	Nodes	VOF/maximum velocity magnitude (m/s)	DPM/D (3,2) (m)
1	0.005	93770	51904	509	1.520529 e-5
2	0.004	137482	73864	510	1.519298e-5
3	0.003	228900	119746	511	1.517333e-5

(3-3) Setting up

The mesh, properly partitioned, is imported into Fluent for solving. The materials selected are ideal gas and liquid water, with the energy equation activated. The pressure-velocity coupling method adopts the Simple algorithm. The turbulence model chosen is the standard k-ε model, with standard wall functions. Under varied water pressures of 0.1/0.2/0.3/0.4/0.5 MPa, a numerical analysis of the velocity, atomization angle, Mach number, and liquid phase volume fraction in the internal and external flow fields of the linear Laval nozzle is conducted using Fluent's VOF model. This analysis aims to determine the optimal water pressure.

3.2. DPM simulation setup

(1) Governing equation

Using the Lagrangian DPM allows for a more accurate simulation of droplet atomization, providing a more realistic depiction of the process of droplet fragmentation and trajectory. The trajectory of the droplets is determined by solving the differential equations of particle forces in the Lagrangian coordinate system, which are then transformed into equilibrium equations in the Cartesian coordinate system shown in the formula below [22].

$$\frac{du_{p,x}}{dt} = F_D\left(u_{v,x} - u_{p,x}\right) + \frac{g_x\left(\rho_p - \rho_v\right)}{\rho_p} - D_{r,p}\frac{1}{m_p T}\frac{\partial T}{\partial x} \tag{8}$$

$$\frac{du_{p,y}}{dt} = F_D\left(u_{v,y} - u_{p,y}\right) + \frac{g_y\left(\rho_p - \rho_v\right)}{\rho_p} - D_{r,p}\frac{1}{m_p T}\frac{\partial T}{\partial y} \tag{9}$$

$$\frac{du_{p,z}}{dt} = F_D\left(u_{v,z} - u_{p,z}\right) + \frac{g_z\left(\rho_p - \rho_v\right)}{\rho_p} - D_{r,p}\frac{1}{m_p T}\frac{\partial T}{\partial z} \tag{10}$$

where m_p is the particle mass (kg), $D_{T,P}$ is the thermal swimming force coefficient, ρ_v is the fluid density (kg/m^3), ρ_p is the particle density (kg/m^3), u_v is the fluid velocity (m/s), u_p is the particle velocity (m/s), t is the time (s), F_D is the traction force per unit mass of dust (N), g is the acceleration of gravity (m/s^2), T is the fluid temperature (K), and x, y, and z are the coordinates (m).

(2) Domain and Meshing: Like VOM, it will not be introduced here.

(3) Boundary conditions and setting up

The boundary conditions for DPM differ from those of the VOF model. The gas inlet, pressure outlet, exhaust, and wall conditions are the same as in the VOF model. The water inlet of DPM is designed as a particle source, and the particle material is liquid water. An ideal gas is chosen for the gas phase with the energy equation enabled. Pressure-velocity coupling is implemented using the coupled algorithm. The turbulence model employed is the standard k-epsilon model with standard wall functions. Diameter distribution follows the Rosin-Rammler distribution. Droplet parameters are set as indicated in Table 2 [19]. Under varied water pressures of 0.1, 0.2, 0.3, 0.4, and 0.5 MPa, numerical analysis using Fluent's DPM will be conducted to investigate the spray shape and droplet sizes in the outflow field of the Laval nozzle. The velocity magnitude is calculated based on the total flow rate.

Table 2 DPM droplet source settings

Water pressure	0.1 MPa	0.2 MPa	0.3 MPa	0.4 MPa	0.5 MPa
Velocity magnitude (m/s)	2.89	5.37	7.16	9.71	12.84
Total flow rate (kg/s)	0.0010479	0.001949	0.0026008	0.0035258	0.0046638
Maximum particle diameter (mm)	0.04	0.09	0.105	0.125	0.15
Minimum particle diameter (mm)	0.005	0.002	0.001	0.002	0.002
Mean particle diameter (mm)	0.02	0.028	0.031	0.04	0.05

4. Results and Discussion

When the air pressure is 0.5 MPa, the influence of varied water pressure on the spray velocity, atomization angle, and droplet size were analyzed. This study also confirmed the achievement of supersonic flow within the Laval nozzle and analyzed the Mach number at a water pressure of 0.1 MPa.

4.1. Verification of the supersonic effect of the Laval nozzle

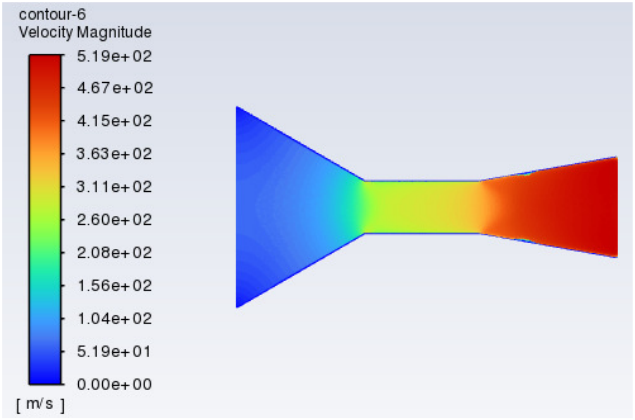

Fig. 14 Contours of velocity magnitude

Fig. 14 shows the contours of the velocity magnitude of the flow field inside the Laval nozzle. In the initial section of the jet, the color of the velocity cloud map is blue, indicating lower velocities. As the flow field contracts, the velocity gradually increases. Upon reaching the throat section, the color of the velocity cloud map changes to yellow, indicating a velocity of approximately 320 m/s, at which point the velocity reaches the speed of sound. After passing through the throat section, the velocity cloud map turns red, indicating an increase in velocity from the speed of sound to supersonic speeds, with the maximum velocity reaching 519 m/s. Furthermore, the airflow remains stable. There are no shock waves within the entire expansion section, and the airflow remains attached to the walls, resulting in no vortex loss and achieving the ideal effect.

As shown in Fig. 15, Yang et al. [1] stated in the paper that the airflow inside the Laval nozzle reaches the speed of sound, consistent with the numerical analysis results in this study. However, Yang et al. [1] do not show the acceleration process; the nozzle should achieve sonic speeds at the throat.

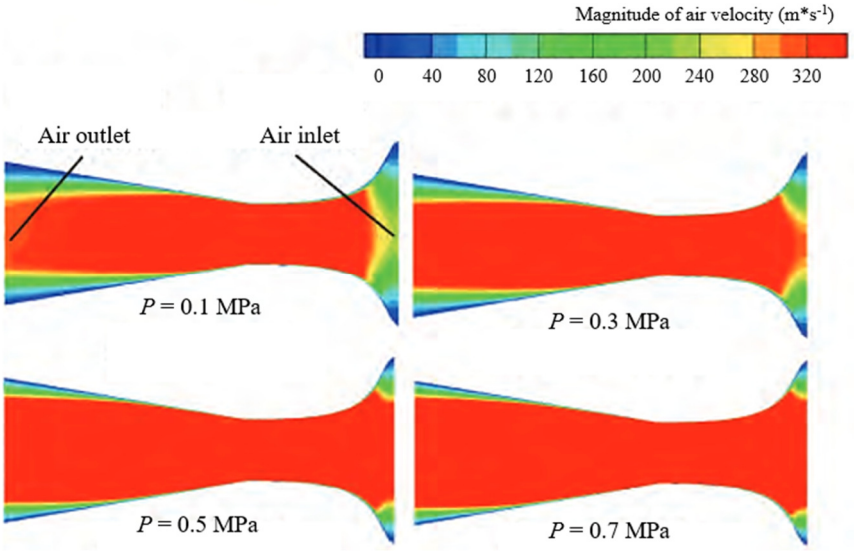

Fig. 15 Numerical analysis of Laval nozzle in Yang's paper [1]

4.2. *Velocity analysis*

The mechanism of spray dust removal is to mist water into tiny droplets, which are sprayed into the air and in contact with floating dust. The main factor affecting the dust-trapping effect of water droplets is the relative speed of water droplets and dust particles, which determines the contact effect between dust and water droplets. The high speed of water droplets leads to sizeable kinetic energy, and the collision with dust particles is conducive to overcoming the surface tension of water and wetting and capturing dust particles more effectively.

Fig. 16 illustrates contours of velocity magnitude under varied water pressures. Water pressure has a significant impact on velocity magnitude as well as the morphology of the flow field. Velocity magnitude is higher near the nozzle, gradually diminishing in the outer flow field. The presence of the oscillator increases the atomization angle and creates vortices near the nozzle outlet, which facilitates atomization. Under varied water pressures, the maximum velocity magnitude of the mixture varies, as shown in Table 3.

Table 3 The velocity magnitude of the mixture under varied water pressures

The air pressure is 0.5 MPa; Water pressure (MPa)	Maximum velocity magnitude of mixture (m/s)
0.1	510
0.2	493
0.3	495
0.4	506
0.5	550

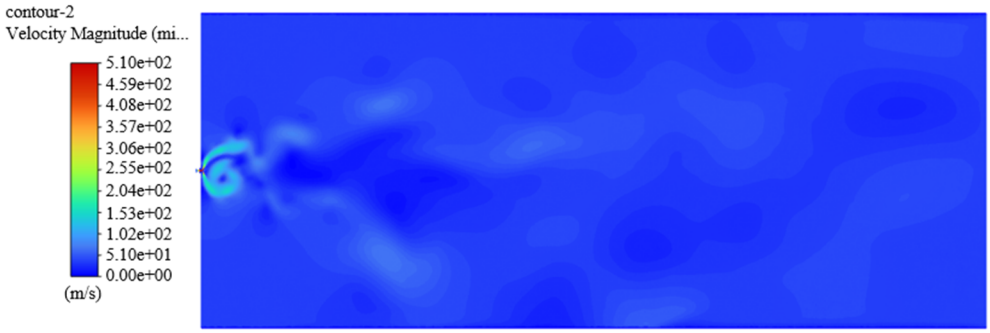

(a) Contours of velocity magnitude at 0.1 MPa water pressure

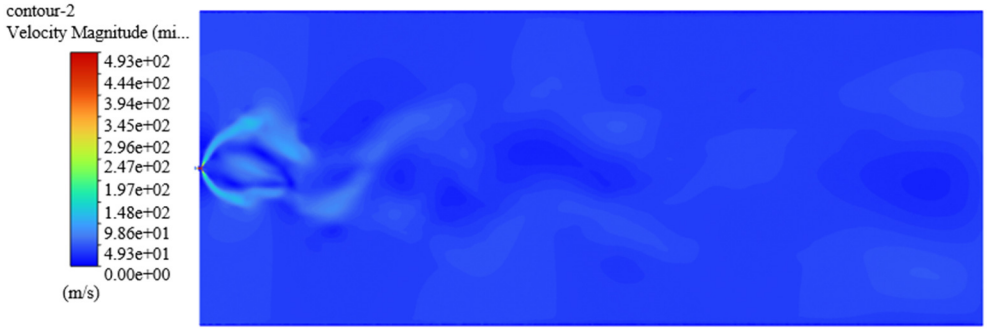

(b) Contours of velocity magnitude at 0.2 MPa water pressure

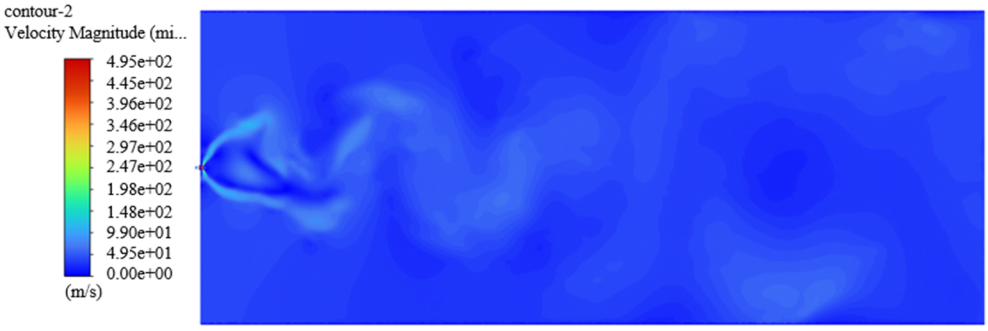

(c) Contours of velocity magnitude at 0.3 MPa water pressure

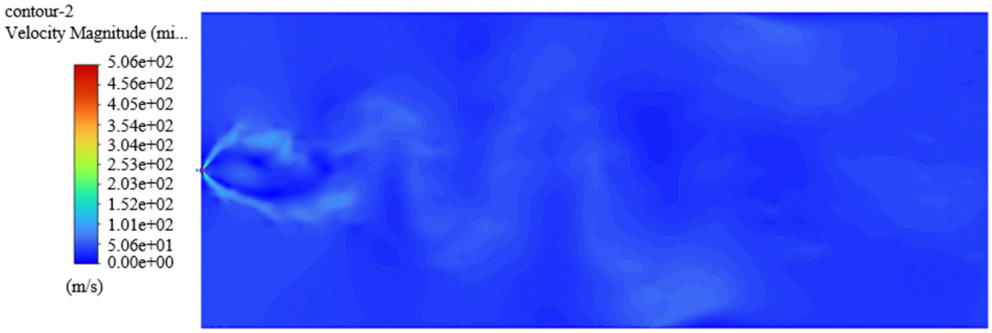

(d) Contours of velocity magnitude at 0.4 MPa water pressure

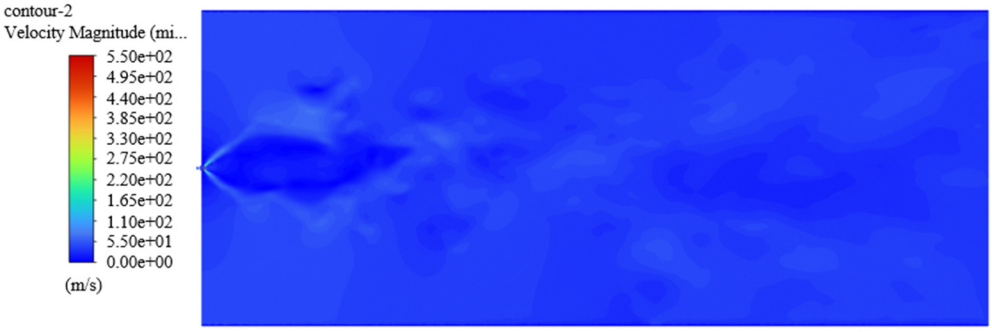

(e) Contours of velocity magnitude at 0.5 MPa water pressure

Fig. 16 Contours of velocity magnitude at varied water pressures

The scatter plot shown in Fig. 17, with water pressure on the x-axis and velocity magnitude on the y-axis, illustrates a decrease and an increase in velocity magnitude as water pressure varies from 0.1 MPa to 0.5 MPa. At a water pressure of 0.5 MPa, the velocity magnitude reaches its maximum, measuring 550 m/s. Then, at a water pressure of 0.1 MPa, the velocity magnitude is 510 m/s. The minimum velocity magnitude is observed at a water pressure of 0.2 MPa, measuring 493 m/s. The fitting curve for velocity magnitude and water pressure is given by the equation: $y = 935.71\ x^2 - 468.433x + 548.4$, $R^2 = 0.983$, demonstrating a good fit.

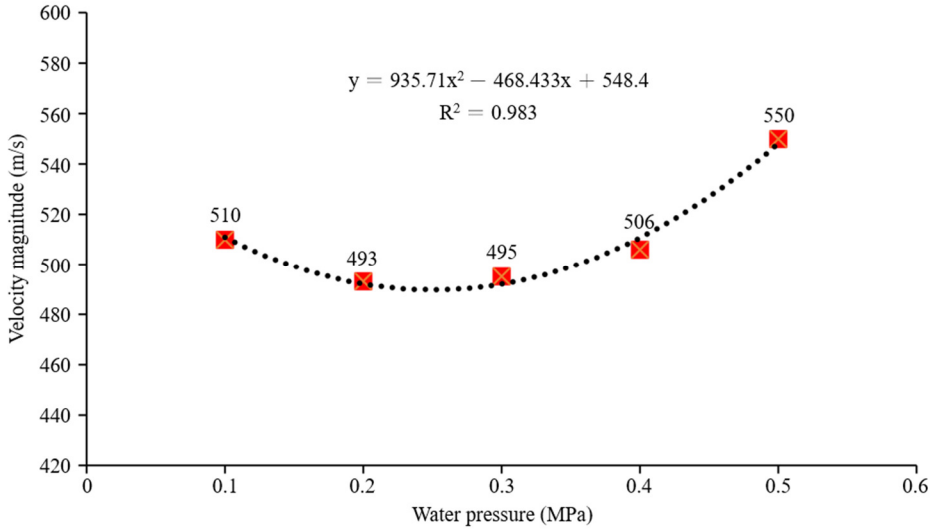

Fig. 17 Scatter plot of velocity magnitude under varied water pressures

The velocity magnitude of the gas-liquid mixture decreases first and then increases. It indicates that when the gap between water pressure and air pressure is relatively large, increasing water pressure will hinder air movement. When the water pressure is close to the air pressure, it promotes the movement of the air. According to the literature, the higher the outlet speed, the better the dust removal effect [1]. So, the water pressure of 0.1 MPa and 0.5 MPa is better.

4.3. Atomization angle analysis

The atomization angle determines the distribution of fluid space to a large extent. As the atomization angle increases, the coverage area expands and the likelihood of collisions with dust particles rises. Therefore, a larger collection area results in more effective dust suppression. Fig. 18 shows the Contours of water volume fraction under varied water pressures. The figure shows that the water volume fraction is lower in the outer flow field due to atomization, especially at lower water pressures. Therefore, in this research, the angle of the contours of velocity magnitude is measured to compare the atomization range under varied water pressures.

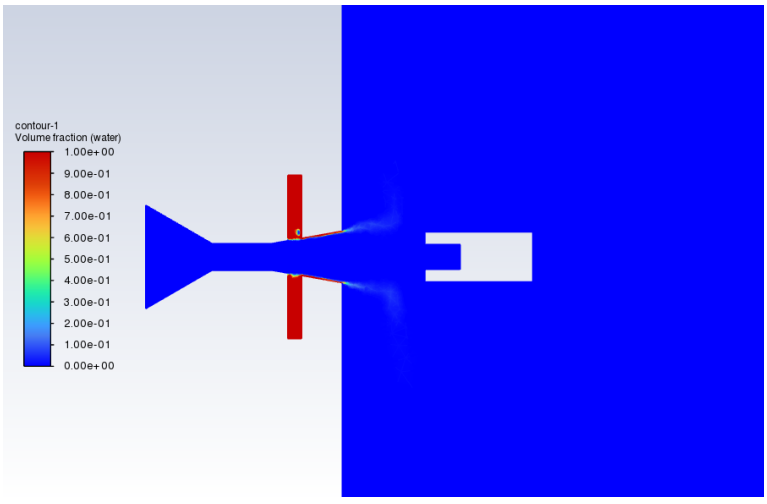

Fig. 18 Contours of water volume fraction at 0.1MPa water pressure

The angle of the atomization range was measured using the Online Protractor tool shown in Fig. 19, which, to some extent, reflects the size of the atomization angle. It is evident from Fig. 19 that as the water pressure increases, the angle of the atomization range decreases. Higher pressure leads to an increase in jet velocity, resulting in droplets with higher kinetic energy. These high-energy droplets follow a more linear trajectory in the air, experiencing less resistance and deviation. So, the droplets move forward in a straight line under higher pressure conditions without quickly deviating, resulting in a smaller atomization angle [23]. The data regarding the angle of atomization range under varied water pressures is listed in Table 4.

Table 4 Angle of atomization range under varied water pressures

The air pressure is 0.5MPa; Water pressure (MPa)	The angle of atomization range (°)
0.1	156
0.2	147
0.3	139
0.4	127
0.5	109

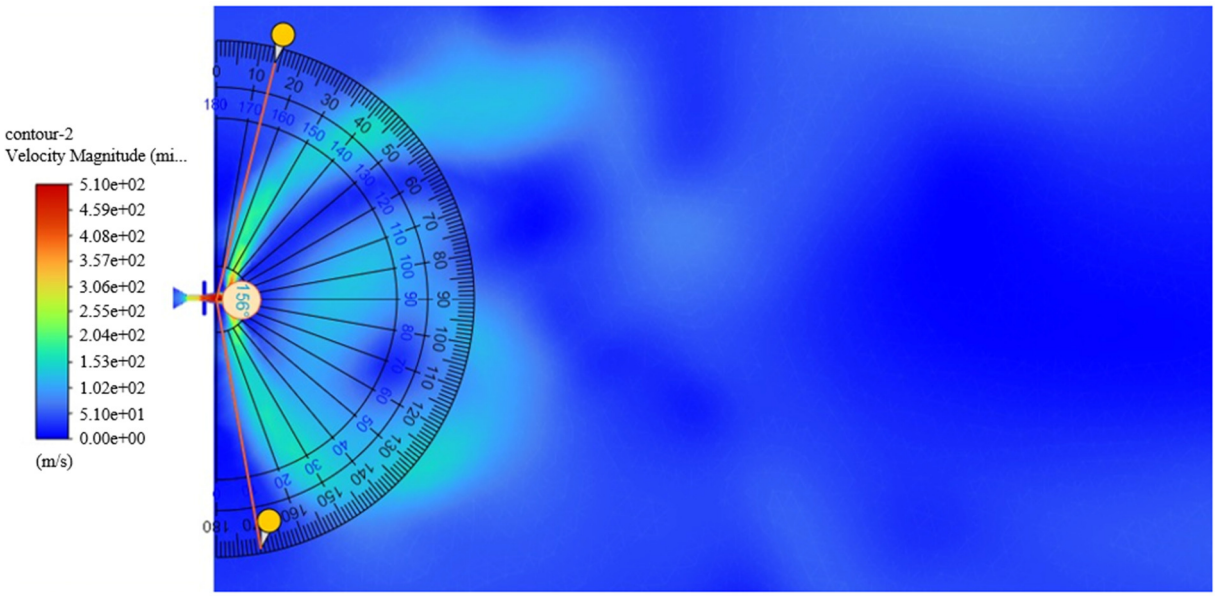

(a) The angle of atomization range at 0.1 MPa water pressure

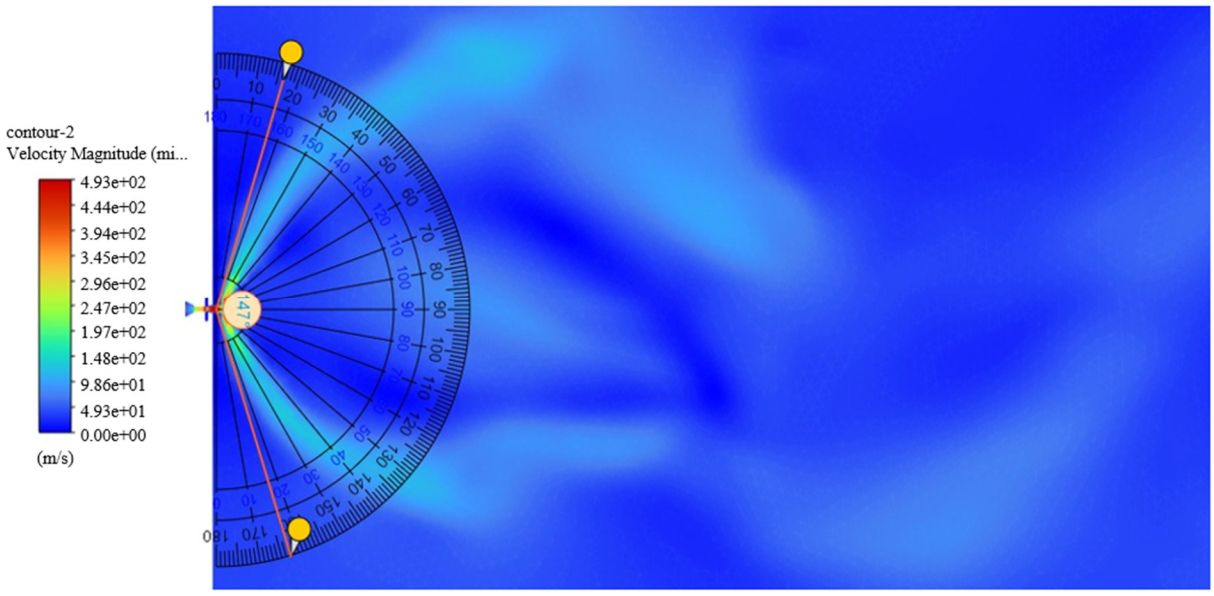

(b) The angle of atomization range at 0.2 MPa water pressure

Fig. 19 Angle of atomization range at varied water pressures

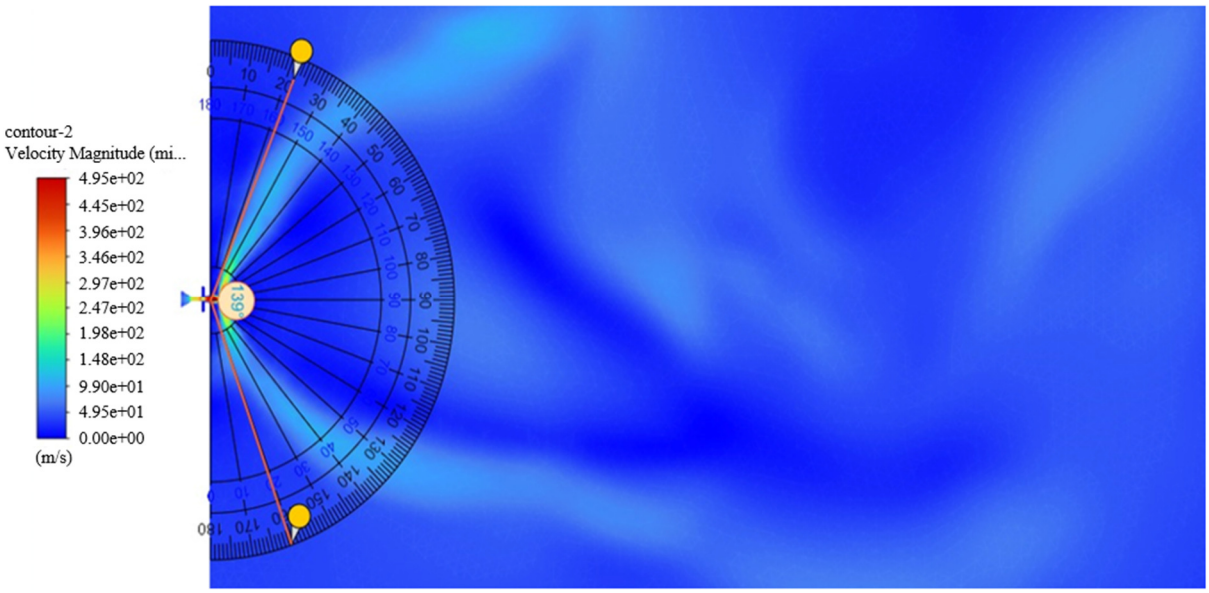

(c) The angle of atomization range at 0.3 MPa water pressure

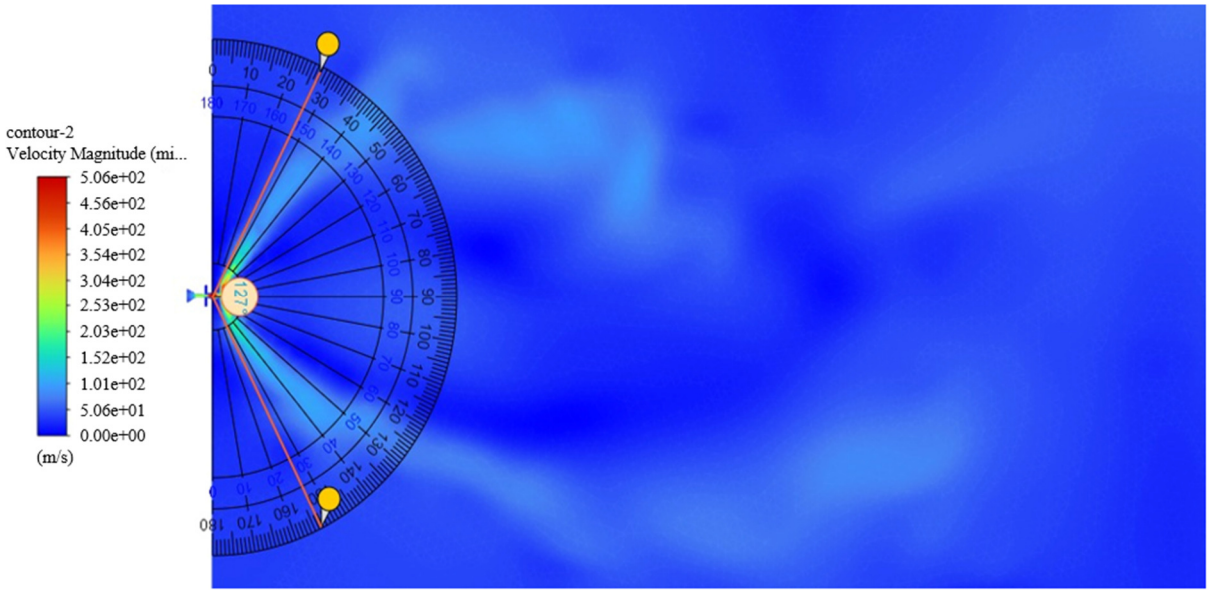

(d) The angle of atomization range at 0.4 MPa water pressure

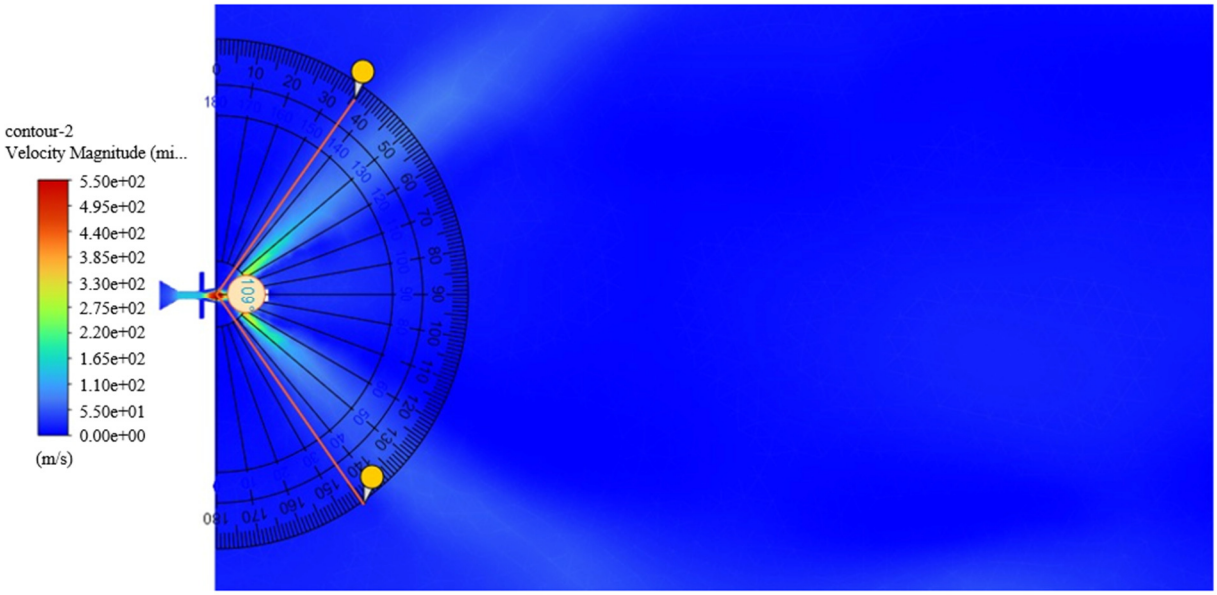

(e) The angle of atomization range at 0.5 MPa water pressure

Fig. 19 Angle of atomization range at varied water pressures (continued)

The scatter plot shown in Fig. 20 with water pressure on the x-axis and angle of atomization range on the y-axis illustrates a decrease in the angle of atomization range as water pressure varies from 0.1 MPa to 0.5 MPa. At a water pressure of 0.1 MPa, the angle of atomization range is at its maximum, measuring 156°, whereas at 0.5 MPa, it decreases to 109°. Therefore, the optimal atomization angle is observed at 0.1 MPa. The fitting curve for the relationship between the angle of atomization range and water pressure is given by y = -114x + 169.8, R^2 = 0.9704, showing a perfect fit.

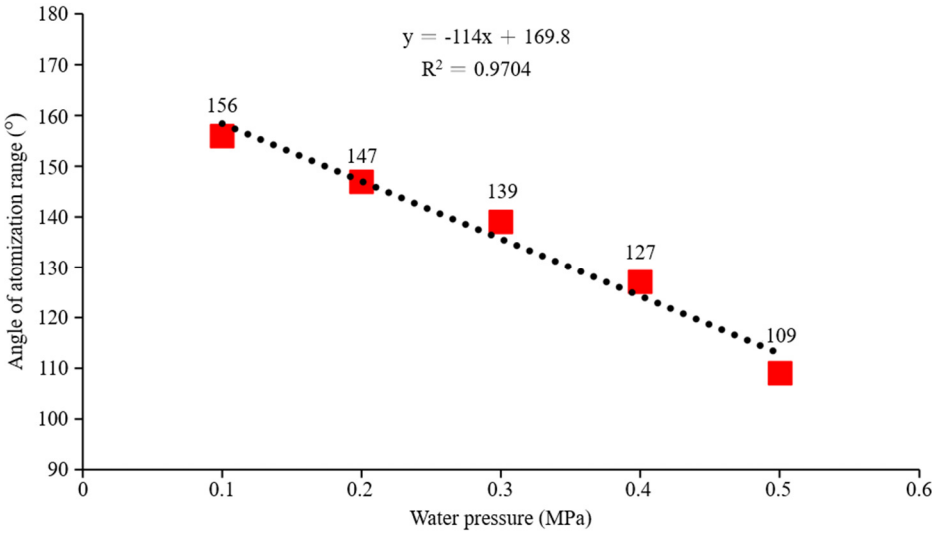

Fig. 20 Scatter plot of the angle of atomization range under varied water pressures

4.4. *Droplet size analysis*

In practical theory and application, the Sauter mean diameter (SMD) is commonly used to represent the droplet size in a fog. The SMD denotes the surface area-weighted mean diameter and is denoted by D (3,2). Its mathematical expression, as given by the formula [24]:

$$D(3,2)=\frac{\sum_{i=1}^{m} n_i \bar{d}_i^{\,2} \times \bar{d}_i}{\sum_{i=1}^{m} n_i \bar{d}_i^{\,2}} \tag{11}$$

$\bar{d}_i$ represents the diameter of each droplet; m is the total number of droplets; $n_i \bar{d}_i^{\,2}$ is directly proportional to the total surface area of particles in the i-size interval; D (3,2) represents the average particle diameter concerning the surface area, known as the surface area mean diameter or the SMD.

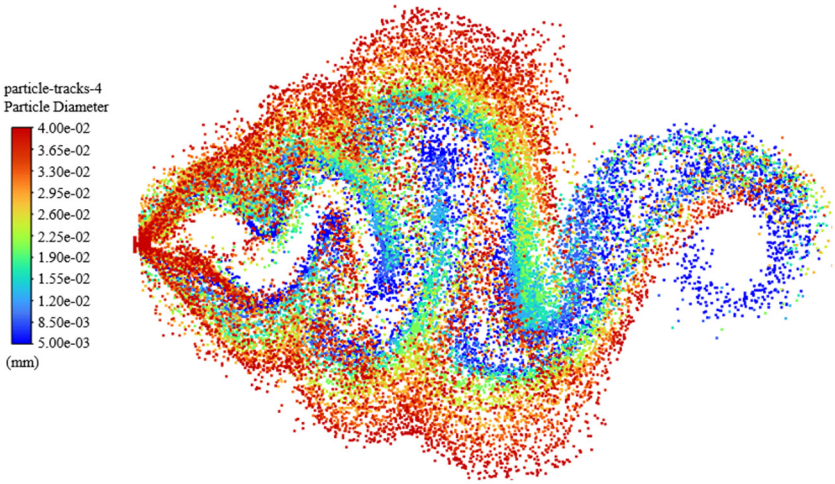

(a) Droplet traces colored by droplet diameter at 0.1 MPa water pressure

Fig. 21 Droplet traces colored by droplet diameter at varied water

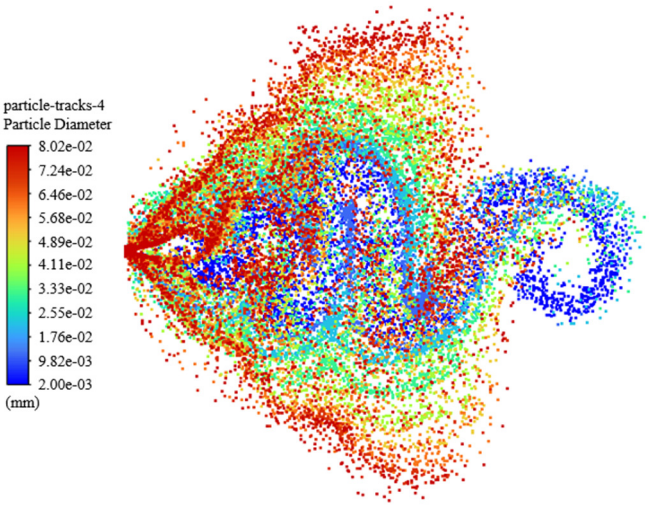

(b) Droplet traces colored by droplet diameter at 0.2 MPa water pressure

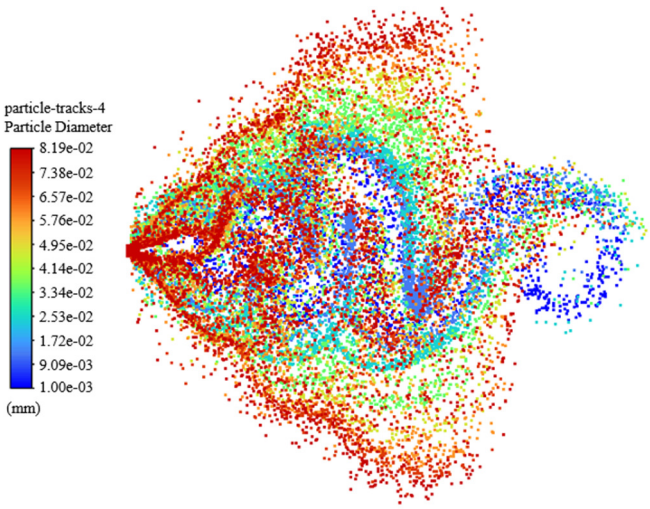

(c) Droplet traces colored by droplet diameter at 0.3 MPa water pressure

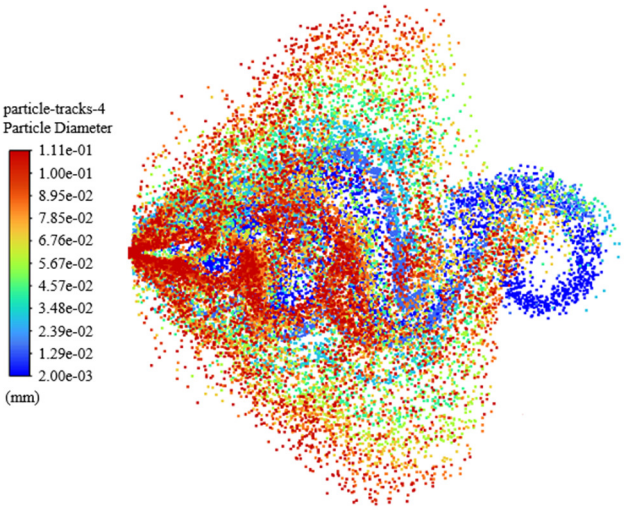

(d) Droplet traces colored by droplet diameter at 0.4 MPa water pressure

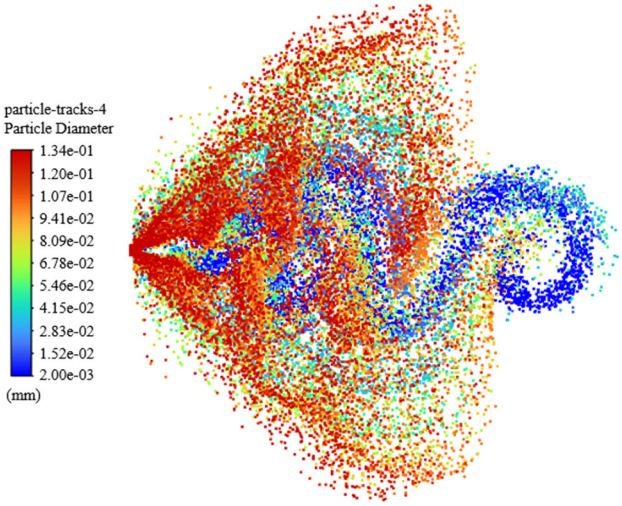

(e) Droplet traces colored by droplet diameter at 0.5 MPa water pressure

Fig. 21 Droplet traces colored by droplet diameter at varied water (continued)

From Fig. 21, it can be observed that droplet traces colored by droplet diameter exhibit similar shapes under varied pressures. Droplets in the middle are smaller, while those on the sides are larger. When the liquid passes through the nozzle, the high-speed airflow shears and impacts the liquid, dispersing it into fine droplets. Because as the spray develops freely, the droplets become more dilute [25]. As water pressure increases, droplet diameters also increase. Increasing water pressure means more liquid is sprayed out, which increases the collision and impact between liquid droplets. This collision leads to the formation of larger droplets [26]. On the other hand, increasing water pressure reduces the atomization angle, shrinking the space for droplet distribution, thereby increasing the probability of collision and impact and enlarging the droplet diameter. In Fluent results reports, statistical droplet size distribution can be displayed. The SMD under varied pressures is shown in Fig. 20.

Table 5 Droplet diameter under varied water pressures (m)

S.No.	D (2,1) Overall surface diameter	D (3,1) Overall volume diameter	D (3,2)/ SMD Overall Sauter diameter	D (4,3) Overall de Brouckere diameter
A	1.213387e-05	1.357754e-05	1.519298e-05	1.773705e-05
B	1.172466e-05	1.556002e-05	2.064999e-05	2.495938e-05
C	9.429700e-05	1.439233e-05	2.196668e-05	2.677897e-05
D	1.156934e-05	1.762769e-05	2.685853e-05	3.447520e-05
E	1.223134e-05	2.073445e-05	3.514886e-05	4.498832e-05

Table 5 illustrates the statistical droplet size distribution under varied water pressures. In practical theory and application, the SMD is commonly used to represent droplet sizes. At an air pressure of 0.5 MPa, the SMD varies under different water pressures (0.1, 0.2, 0.3, 0.4, and 0.5 MPa). The smallest SMD is observed at a water pressure of 0.1 MPa. The specific values are shown in Table 6.

Table 6 Sauter mean diameter under varied water pressures

The air pressure is 0.5 MPa; Water pressure (MPa)	D (3,2) — Sauter mean diameter (m)
0.1	1.519298e-5
0.2	2.064999e-5
0.3	2.196668e-5
0.4	2.685863e-5
0.5	3.514886e-5

The scatter plot shown in Fig. 22 with water pressure on the x-axis and SMD on the y-axis illustrates an increase in SMD as water pressure varies from 0.1 MPa to 0.5 MPa. At a water pressure of 0.1 MPa, the SMD is at its minimum, measuring 15.19 μm, whereas at 0.5 MPa, it increases to 35.15 μm. Therefore, the optimal SMD is observed at 0.1 MPa. The fitting curve for the relationship between SMD and water pressure is given by $y = 46.13x + 10.125$, $R^2 = 0.9439$, showing a good fit.

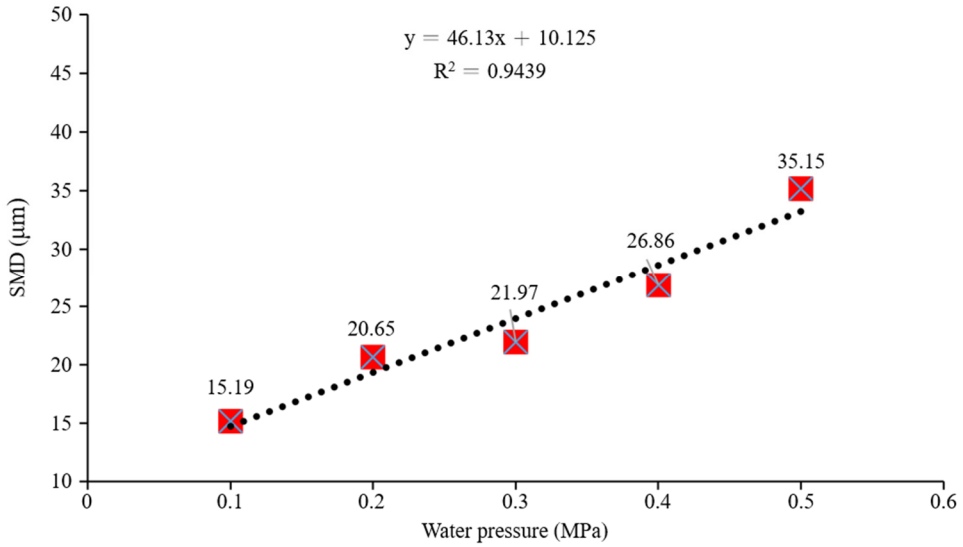

Fig. 22 Scatter plot of Sauter mean diameter (SMD) under varied water pressures

4.5. *Mach number analysis*

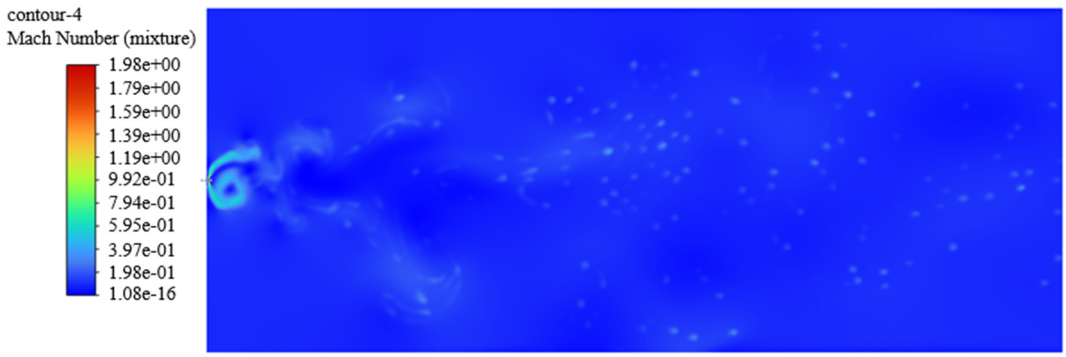

Fig. 23 Contours of Mach number at 0.1 MPa water pressure

As shown in Fig. 23, when the water pressure is 0.1 MPa, the Mach number is 1.98. Many points in the outflow field with relatively high Mach numbers indicate the presence of numerous vortices, which are conducive to atomization. In summary, at an air pressure of 0.5 MPa, spray velocities are optimal at both 0.1 MPa and 0.5 MPa water pressures. At 0.1 MPa water

pressure, the atomization cone angle is the largest, and the droplet size is the smallest. The Mach number plot indicates that at 0.1 MPa water pressure, the presence of vortices in the spray field aids atomization. Therefore, at an air pressure of 0.5 MPa, a water pressure of 0.1 MPa is optimal.

5. Research Contribution

Table 7 compares water pressure between the traditional nozzle and the optimized Laval nozzle. Traditional pressure-rotating nozzles typically operate at water pressures exceeding 5 MPa. Such high-pressure demands increase energy consumption, substantial water usage, elevated costs, and potential safety hazards. In contrast, the optimized Laval nozzle utilized in this study operates at a water pressure of 0.1 MPa, representing a reduction of over 90% compared to traditional nozzles. This results in energy efficiency, cost-effectiveness, and improved safety measures.

Table 7 The comparison of water pressure between the traditional nozzle and the optimized Laval nozzle

Reference	Nozzle type	Water pressure (MPa)
Xu et al., [5] (2019)	Pressure swirling nozzle	8
Liu et al., [4] (2019)	Press-swirl nozzle	5
This research	Laval nozzle	0.1

Table 8 compares the spray angle between the traditional nozzle and the optimized Laval nozzle. Typically, traditional nozzles have a maximum spray angle of around 60°, while the optimized Laval nozzle in this research can achieve a theoretical maximum spray cone angle of 156°. This represents an increase of approximately 150% in the spray angle compared to traditional nozzles. A larger spray angle allows for a more extensive dispersion of droplets, covering a larger area and facilitating a more uniform distribution, thereby enhancing dust removal efficiency.

Table 8 The comparison of spray angle between traditional nozzles and optimized Laval nozzles

Reference	Nozzle type	Spray angle (°)
Zhang et al., [10] (2020)	Ultrasonic nozzle	61.5
Amoli et al., [27] (2022)	A spray nozzle	60
This research	Laval nozzle	156

Table 9 compares droplet size D (3,2) between traditional pressure-swirl nozzles and optimized Laval nozzles. Droplets generated by traditional pressure-swirl nozzles typically exceed 50 μm in diameter, while the optimal D (3,2) achieved with the Laval nozzle used in this research is only 15.2 μm, representing a reduction of over 50%. When the diameter of droplets is similar to that of dust particles, the dust removal efficiency is significantly improved. Therefore, the small-diameter droplets produced by the Laval nozzle are advantageous for enhancing respirable dust removal efficiency.

Table 9 The comparison of droplet size D (3,2) between traditional nozzles and optimized Laval nozzles

Reference	Nozzle type	Droplet size D (3,2) (μm)
Liu et al., [4] (2019)	Press-swirl nozzle	90
Xu et al., [6] (2020)	pressure-swirl nozzle	51
This research	Laval nozzle	15.2

6. Conclusion

This research focuses on the study of linear Laval nozzles, investigating the influence of operating conditions (water pressure) on atomization performance. The main findings are summarized as:

(1) The VOF model simulates the nozzle's internal and external fields and analyzes the velocity and atomization angle as water pressure varies from 0.1 MPa to 0.5 MPa. At a water pressure of 0.5 MPa, the velocity magnitude reaches its maximum, measuring 550 m/s. And, at a water pressure of 0.1 MPa, the velocity magnitude is 510 m/s. The fitting curve for velocity magnitude and water pressure is given by the equation: $y = 935.71\ x^2 – 468.43x + 548.4$, $R^2 = 0.983$. On the

other hand, at a water pressure of 0.1 MPa, the angle of the atomization range is at its maximum, measuring 156°. The fitting curve for the relationship between the angle of atomization range and water pressure is given by $y = - 114x + 169.8$, $R^2 = 0.9704$.

(2) DPM of Fluent is used to analyze the droplet size of the spray as water pressure varies from 0.1 MPa to 0.5 MPa. At a water pressure of 0.1 MPa, the SMD is at its minimum, measuring 15.19 μm. The fitting curve for the relationship between SMD and water pressure is given by $y = 46.13x + 10.125$, $R^2 = 0.9439$.

(3) At an air pressure of 0.5 MPa, a water pressure of 0.1 MPa is optimal. Compared to traditional nozzles, the water pressure is reduced by over 90%, and D (3,2) decreases by over 50%. Moreover, the theoretical spray angle increases by approximately 150% with the linear Laval nozzle, leading to significantly enhanced atomization performance.

(4) The linear Laval nozzle studied in this research is easy to manufacture, exhibits excellent atomization performance, operates at low pressure, and is cost-effective.

Notably, a combination-type nozzle is proposed, which expands the atomization angle. These nozzles produce dry mist due to the small droplet size. Compared to traditional water mist dust removal methods, they are more energy-efficient and environmentally friendly, as they do not require large amounts of water resources and do not lead to groundwater accumulation or secondary pollution. Dry mist dust removal does not involve water, thus avoiding safety hazards such as slipping and electrical equipment failures caused by water mist. The linear nozzles are applicable in diverse enclosed environments such as mines, construction sites, and processing plants. They can reduce dust removal efficiency effectively, significantly contributing to human health and environmental protection.

Acknowledgment

This research was funded by the Key Project of the Anhui Natural Science Foundation, 2024AH050525.

Conflicts of Interest

The authors declare no conflict of interest.

References

[1] C. Yang, B. Chen, W. Jiang, D. Gao, and G. Jin, "Analysis and Experiment on Atomizing Characteristics of Supersonic Nozzle Based on Laval Effect," Transactions of the Chinese Society of Agricultural Engineering, vol. 32, no. 19, pp. 57-64, October 2016.

[2] S. Tang, M. D. Ibrahim, A. R. H. Rigit, W. Zhang, and C. Wei, "A Systematic Review of Dust Suppression Methods by Experiment Based on Intelligent Technology in the Coal Mines," Journal of Electrical Systems, vol. 20, no. 3, pp. 882-893, 2024.

[3] F. Anlimah, V. Gopaldasani, C. MacPhail, and B. Davies, "A Systematic Review of the Effectiveness of Dust Control Measures Adopted to Reduce Workplace Exposure," Environ Sci Pollut Res, vol. 30, no. 19, pp. 54407-54428, April 2023.

[4] Z. Liu, W. Nie, H. Peng, S. Yang, D. Chen, and Q. Liu, "The Effects of the Spraying Pressure and Nozzle Orifice Diameter on the Atomizing Rules and Dust Suppression Performances of an External Spraying System in a Fully-Mechanized Excavation Face," Powder Technology, vol. 350, pp. 62-80, May 2019.

[5] C. Xu, W. Nie, Z. Liu, H. Peng, S. Yang, and Q. Liu, "Multi-Factor Numerical Simulation Study on Spray Dust Suppression Device in Coal Mining Process," Energy, vol. 182, pp. 544–558, Sep. 2019.

[6] C. Xu, W. Nie, S. Yang, H. Peng, Z. Liu, Q. Ma, et al., "Numerical Simulation of the Multi-Index Orthogonal Experiments on the Spray Dust-Settling Devices," Powder Technology, vol. 371, pp. 217-230, June 2020.

[7] S. Arya, J. Sottile, and T. Novak, "Numerical Modeling of a Flooded-Bed Dust Scrubber Integrated into a Longwall Shearer," Mining, Metallurgy & Exploration, vol. 37, no. 4, pp. 1105-1119, August 2020.

[8] Y. Shi, P. Wang, R. Liu, X. Tan, and W. Zhang, "Numerical Simulation and Engineering Application of Coalbed Water Injection," Mathematical Problems in Engineering, vol. 2019, article no. 6309160, 2019.
[9] P. Wang, H. Han, R. Liu, R. Gao, and G. Wu, "Effect of Outlet Diameter on Atomization Characteristics and Dust Reduction Performance of X-Swirl Pressure Nozzle," Process Safety and Environmental Protection, vol. 137, pp. 340-351, May 2020.
[10] T. Zhang, D. Jing, S. Ge, J. Wang, X. Chen, and S. Ren, "Dust Removal Characteristics of a Supersonic Antigravity Siphon Atomization Nozzle," Advances in Mechanical Engineering, vol. 12, no. 12, article no. 1687814020977689, 2020.
[11] T. Zhang, D. Jing, S. Ge, J. Wang, and X. Chen, "Supersonic Antigravity Aerodynamic Atomization Dusting Nozzle Based on the Laval Nozzle and Probe Jet," Journal of the Brazilian Society of Mechanical Sciences and Engineering, vol. 42, no. 6, article no. 335, June 2020.
[12] O. Dumitrescu, B. Gherman, and T. Tipa, "Development of a Laval Nozzle for a Cold Gas Propulsion System," IOP Conference Series: Materials Science and Engineering, vol. 400, no. 4, article no. 042016, 2018.
[13] Y. Liu, J. Zhang, J. Wei, and X. Liu, "Optimum Structure of a Laval Nozzle for an Abrasive Air Jet Based on Nozzle Pressure Ratio," Powder Technology, vol. 364, pp. 343-362, March 2020.
[14] G. Lai and W. Sheng, "Supersonic Reacting Jet Flows from a Three-Dimensional Divergent Conical Nozzle," SIAM Journal on Mathematical Analysis, vol. 55, no. 5, pp. 5260-5317, 2023.
[15] O. Durif, "Design of de Laval Nozzles for Gas-Phase Molecular Studies in Uniform Supersonic Flow," Physics of Fluids, vol. 34, no. 1, article no. 013605, January 2022.
[16] O. O. Mil'man, A. S. Goldin, B. A. Shifrin, V. B. Perov, L. N. Serezhkin, A. V. Ptakhin, et al., "Experimental Investigation into Performance of Laval Nozzles for Reaction Turbines," Thermal Engineering, vol. 70, no. 12, pp. 1083-1101, December 2023.
[17] Q. Xu and J. Xie, "Numerical Simulation of the Effect of Different Numbers of Inlet Nozzles on Vortex Tubes," Processes, vol. 9, no. 9, article no. 1531, September 2021.
[18] Y. Xu, Q. Li, B. Li, and Z. Guan, "Numerical Simulation Study of Hydraulic Fracturing Nozzle Erosion in Deep Well," Frontiers in Physics, vol. 10, article no. 947094, 2022.
[19] H. Ou, L. Su, Y. Shi, and S. Ruan, "Investigation on High-Viscosity Chemical Waste Liquid Atomizer Based on VOF-DPM," Energies, vol. 16, no. 7, article no. 3109, April 2023.
[20] I. A. Fetuga, O. T. Olakoyejo, S. M. Abolarin, A. O. Adelaja, S. O. Ologunoba, O. Oluwatusin, et al., "Eulerian–Lagrangian Fluid Dynamics Study on the Effects of Inlet Radial Angle on the Performance and Flow Pattern of Multi-Inlet Cyclone Separator," Alexandria Engineering Journal, vol. 78, pp. 453-468, September 2023.
[21] Q. Zeng, S. Zhu, Z. Li, and X. Guo, "Self-Adaptive Triangular Mesh Generation Framework for Free-Form Single-Layer Reticulated Shells Based on Virtual Interaction Forces," Automation in Construction, vol. 148, article no. 104750, April 2023.
[22] T. Zhao, C. Chen, X. Liu, and J. Hao, "Effect of Gas Mach Number on the Flow Field of Close-Coupled Gas Atomization, Particle Size and Cooling Rate of As-Atomized Powder: Simulation and Experiment," Advanced Powder Technology, vol. 34, no. 5, article no. 104007, May 2023.
[23] Y. Wang, Z. Jiang, F. Zhang, Y. Lu, and Y. Bao, "Study on Dust Diffusion Characteristics of Continuous Dust Sources and Spray Dust Control Technology in Fully Mechanized Working Face," Powder Technology, vol. 396, part B, pp. 718-730, January 2022.
[24] L. Li, A. Chen, T. Deng, J. Zeng, F. Xu, S. Yan, et al., "A Simple Optical Aerosol Sensing Method of Sauter Mean Diameter for Particulate Matter Monitoring," Biosensors, vol. 12, no. 7, article no. 436, July 2022.
[25] Z. Feng, C. Tang, Y. Yin, P. Zhang, and Z. Huang, "Time-Resolved Droplet Size and Velocity Distributions in a Dilute Region of a High-Pressure Pulsed Diesel Spray," International Journal of Heat and Mass Transfer, vol. 133, pp. 745-755, April 2019.
[26] N. S. Atiqah, A. I. M. Shaiful, M. R. Rahim, and N. A. Shuaib, "Bio-Kerosene from Palm Based Fuel: Study of Spray Droplet Size," AIP Conference Proceedings, vol. 2339, no. 1, article no. 020226, May 2021.
[27] B. Siavash Amoli, S. S. Mousavi Ajarostaghi, K. Sedighi, and M. Aghajani Delavar, "Evaporative Pre-Cooling of a Condenser Airflow: Investigation of Nozzle Cone Angle, Spray Inclination Angle and Nozzle Location," Energy Sources, Part A: Recovery, Utilization, and Environmental Effects, vol. 44, no. 3, pp. 8040-8059, 2022.